Monthly Notices
of the
ROYAL ASTRONOMICAL SOCIETY

MNRAS **469,** 787–799 (2017)
Advance Access publication 2017 April 1

doi:10.1093/mnras/stx785

# On the linearity of tracer bias around voids

Giorgia Pollina,[1,2★] Nico Hamaus,[1] Klaus Dolag,[1,3] Jochen Weller,[1,2,4] Marco Baldi[5,6,7] and Lauro Moscardini[5,6,7]

[1]*Universitäts-Sternwarte München, Fakultät für Physik, Ludwig-Maximilians Universität München, Scheinerstr. 1, D-81679 München, Germany*
[2]*Excellence Cluster Universe, Boltzmannstr. 2, D-85748 Garching, Germany*
[3]*Max-Planck-Institute for Astrophysics, Karl-Schwarzschild Strasse 1, D-85748 Garching, Germany*
[4]*Max-Planck Institute for Extraterrestrial Physics, Giessenbachstr. 1, D-85748 Garching, Germany*
[5]*Dipartimento di Fisica e Astronomia, Alma Mater Studiorum Università di Bologna, viale Berti Pichat, 6/2, I-40127 Bologna, Italy*
[6]*INAF - Osservatorio Astronomico di Bologna, via Ranzani 1, I-40127 Bologna, Italy*
[7]*INFN - Sezione di Bologna, viale Berti Pichat 6/2, I-40127 Bologna, Italy*

Accepted 2017 March 28. Received 2017 March 28; in original form 2016 October 20

**ABSTRACT**

The large-scale structure of the Universe can be observed only via luminous tracers of the dark matter. However, the clustering statistics of tracers are biased and depend on various properties, such as their host-halo mass and assembly history. On very large scales, this tracer bias results in a constant offset in the clustering amplitude, known as *linear bias*. Towards smaller non-linear scales, this is no longer the case and tracer bias becomes a complicated function of scale and time. We focus on tracer bias centred on cosmic voids, i.e. depressions of the density field that spatially dominate the Universe. We consider three types of tracers: galaxies, galaxy clusters and active galactic nuclei, extracted from the hydrodynamical simulation *Magneticum* Pathfinder. In contrast to common clustering statistics that focus on auto-correlations of tracers, we find that void–tracer cross-correlations are successfully described by a linear bias relation. The tracer-density profile of voids can thus be related to their matter-density profile by a single number. We show that it coincides with the linear tracer bias extracted from the large-scale auto-correlation function and expectations from theory, if sufficiently large voids are considered. For smaller voids we observe a shift towards higher values. This has important consequences on cosmological parameter inference, as the problem of unknown tracer bias is alleviated up to a constant number. The smallest scales in existing data sets become accessible to simpler models, providing numerous modes of the density field that have been disregarded so far, but may help to further reduce statistical errors in constraining cosmology.

**Key words:** cosmology: theory – large-scale structure of Universe – dark matter – methods: numerical.

## 1 INTRODUCTION

In the present standard cosmological model the large-scale structure of the Universe forms in a hierarchical process that begins with the gravitational collapse of overdense fluctuations of the matter-density field into virialized and gravitationally bound objects, known as dark matter haloes. Such objects provide the potential wells in which baryons can cool and condense to create galaxies that are now observed in the sky (Peebles 1980). The understanding of modern cosmology and structure formation is thereby deeply connected to the statistical properties of dark matter haloes and their hosted galaxies, which represent the final stage of the evolution of primordial fluctuations and can be directly observed and used to constrain theory. Studying the clustering properties of galaxies, it was discovered that they do not precisely mirror the clustering of the bulk of the dark matter distribution: such evidence brought Kaiser (1984) to introduce the concept of galaxy bias to indicate that galaxies are biased tracers of the underlying matter-density field. Kaiser (1984) showed that clusters of galaxies would naturally have a large bias, being rare objects that grow from the highest density peaks in the mass distribution. Bias is now a known property of luminous tracers on very large scales, where density fluctuations are within the linear regime: in this case tracer bias is a simple constant offset in the clustering amplitude, known as *linear bias*. Towards small scales, this elementary relation does not stand and bias becomes an unestablished function of scale and time.

In this paper we focus on the bias of tracers inside and around cosmic voids, large underdense regions in the large-scale structure of the Universe that, together with clusters, filaments and walls define

★ E-mail: giorgia.pollina@gmail.com

the topology of the cosmic web as predicted in a cold dark matter (CDM) cosmology (Bond, Kofman & Pogosyan 1996; Pogosyan et al. 1998). Voids are another peculiarity of the large-scale structure of the Universe, representing the result of the evolution of underdensities in the primordial density field. Although the existence of voids has been one of the earliest predictions of the standard cosmological model (Hausman, Olson & Roth 1983), and the observational discovery of voids dates back to almost 40 years ago (see Gregory, Thompson & Tifft 1978; Kirshner et al. 1981), systematic studies about voids have become possible only recently. This is thanks to the increasing depth and volume of current galaxy surveys which map out larger and larger portions of the sky, and to the advent of large cosmological simulations that are now capable of predicting the distribution of matter in the cosmic web with very high accuracy.

The growing interest for cosmic voids in the literature is partly due to their not yet fully explored potential to constrain cosmology. Voids are the largest structures in the Universe and occupy most of its volume (Cautun et al. 2014; Falck & Neyrinck 2015); their spherically averaged density profile exhibits a universal shape that can be described by a simple empirical function (see e.g. Colberg et al. 2005; Ricciardelli, Quilis & Planelles 2013; Hamaus, Sutter & Wandelt 2014c; Ricciardelli, Quilis & Varela 2014). According to the cosmological principle, they represent a population of statistically ideal spheres with a homogeneous distribution in the Universe at different redshifts, so that their observed shape evolution can be used to probe the expansion history of the Universe by means of the Alcock & Paczynski (AP) test (Alcock & Paczynski 1979), as already demonstrated by recent works (Lavaux & Wandelt 2012; Sutter et al. 2012b, 2014c; Hamaus et al. 2014a, 2016; Mao et al. 2017).

Void counts have the potential to improve upon current constraints on dark energy (DE; Pisani et al. 2015) and can provide a test to discriminate between competing cosmological models. In fact, as their ordinary matter content is by definition very low, voids are expected to be most sensitive to the nature of DE and the features of the primordial density field in which they grow (Odrzywołek 2009; D'Amico et al. 2011; Bos et al. 2012; Gibbons et al. 2014). It has been argued that the shape of voids is particularly sensitive to the equation of state of the DE component (Lavaux & Wandelt 2010). In addition, void abundance and void lensing are possible probes to test for modifications of gravity (Li 2011; Clampitt, Cai & Li 2013; Barreira et al. 2015; Cai, Padilla & Li 2015; Zivick et al. 2015), couplings between dark matter and DE (Pollina et al. 2016), the impact of massive neutrinos on structure formation (Massara et al. 2015) and possible degeneracies between modifications of gravity and warm dark matter particle candidates (Baldi & Villaescusa-Navarro 2016). Although still controversial, it has been investigated whether the observed Cold Spot in the Cosmic Microwave Background could be explained as Integrated Sachs–Wolfe (ISW) imprint caused by very large voids along the line of sight (see e.g. Rees, Sciama & Stobbs 1968; Finelli et al. 2014; Kovač et al. 2014; Nadathur et al. 2014) and, in general, the potential of the ISW effect in voids is still under investigation (Kovács & Granett 2015; Kovács & García-Bellido 2016; Naidoo, Benoit-Lévy & Lahav 2016). Finally, the clustering statistics of voids open up new opportunities to study cosmology (Chan, Hamaus & Desjacques 2014; Hamaus et al. 2014b; Clampitt, Jain & Sánchez 2016; Liang et al. 2016). For example, the Baryon Acoustic Oscillation feature has recently been detected in the auto-correlation function of voids (Kitaura et al. 2016), providing a standard ruler from the underdense regime of the Universe.

All of these studies suggest voids can be considered as promising cosmological probes. Despite that, a lack of understanding in how to link void properties to theory, simulations and observations persists. For what concerns the theoretical comprehension of voids, one of the pioneering works in the field is presented in Sheth & van de Weygaert (2004), where the authors provide a theory to model the void–size distribution and its evolution assuming spherical initial conditions, as commonly done in void evolution models (Peebles 1980; Blumenthal et al. 1992). However, assuming voids to start evolving from spherical underdensities might not be representative of objects developing from Gaussian underdense fluctuations of arbitrary shape. The number function of voids identified in cosmological simulations is in fact not well represented by the model proposed by Sheth & van de Weygaert (2004), as recently argued (see e.g. Jennings, Li & Hu 2013; Nadathur & Hotchkiss 2015b; Falck & Neyrinck 2015; but see Pisani et al. 2015, for how to take this into account). Many studies have been conducted to better understand the evolution of voids over cosmic time (Achitouv, Neyrinck & Paranjape 2015; Demchenko et al. 2016; Wojtak, Powell & Abel 2016) and their number function (Pycke & Russell 2016).

Similarly, another gap that still has to be bridged concerns the relation between the properties of voids in simulations with potentially observable voids. Numerous catalogues of voids identified in spectroscopic data are now available (see e.g. Pan et al. 2012; Sutter et al. 2012a; Ceccarelli et al. 2013; Nadathur 2016; Mao et al. 2017) and recently the largest galaxy survey to date, the Dark Energy Survey, has detected a trough and void lensing signal in a photometric survey of galaxies (Gruen et al. 2016; Sánchez et al. 2017a), opening up new possibilities to exploiting the potential of voids in observations. In the future the next generation of large galaxy surveys, such as the ESA Euclid mission (Laureijs et al. 2011; Amendola et al. 2013), is expected to provide a tremendous amount of new information concerning the large-scale structure of the Universe. The detection of gravitational lensing from medium-sized voids in these surveys will possibly constrain the void density profiles without having to rely on luminous tracers like galaxies, which would require to model their bias (Izumi et al. 2013; Krause et al. 2013; Melchior et al. 2014; Clampitt & Jain 2015). Nevertheless, the vast majority of available void-finders (see e.g. Padilla, Ceccarelli & Lambas 2005; Platen, van de Weygaert & Jones 2007a; Neyrinck 2008; Sutter et al. 2015) rely on the position of dark matter particles in simulations, which cannot be directly compared to observables. The same finders can be adapted to use galaxies as tracers but one will eventually need to model the tracer bias to compare observational results with predictions from simulations and to fully understand properties of voids in the dark matter. For example, several recent works study how redshift-space distortions around void centres provide constraints on cosmological parameters (Hamaus et al. 2015, 2016; Achitouv et al. 2017; Cai et al. 2016; Chuang et al. 2016; Hawken et al. 2016): all of these analyses are based on the assumption that bias is linear in void environments. Nonetheless, a detailed study to investigate and validate this assumption is still missing.

In this paper we aim to directly determine the relation between luminous tracers of the large-scale structure [such as galaxies, clusters and active galactic nuclei (AGN)] and their underlying matter distribution in voids to directly test the linear bias assumption. Thanks to state-of-the-art simulations that feature a full hydrodynamical treatment, the so-called *Magneticum Pathfinder* simulations (Dolag et al., in preparation; see also Hirschmann et al. 2014; Saro et al. 2014; Dolag, Komatsu & Sunyaev 2016; Teklu et al. 2015;

Remus, Burkert & Dolag 2017), we are able to perform this test with very high accuracy. The general idea is to run a void finder on samples of luminous objects and to extract both the distribution of luminous tracers and matter around void centres, in order to compare them against each other.

The paper is organized as follows: in Section 2, we describe the simulations employed in this work; in Section 3, we present the commonly used bias estimators in observations and theory and discuss the void-finder we employ; in Section 4, we explain how we conducted our analysis and in Section 5, we recap all of our results and draw our conclusions.

## 2 THE SIMULATIONS

The *Magneticum Pathfinder*[1] simulations (Dolag et al., in preparation) have already been successfully used in a wide range of numerical studies, showing good agreement with observational findings for the pressure profiles of the intra-cluster medium (Planck Collaboration V et al. 2013; McDonald et al. 2014), the predicted Sunyaev Zeldovich signal (Dolag et al. 2016), the imprint of the intergalactic medium on to the dispersion signal of Fast Radio Bursts (Dolag et al. 2015), the properties of active galactic nuclei (AGN) population (Hirschmann et al. 2014; Steinborn et al. 2015, 2016), the dynamical properties of massive spheroidal galaxies (Remus et al. 2013; Remus, Burkert & Dolag 2017) and for the angular momentum properties of galaxies (Teklu et al. 2015). In this paper we use the largest cosmological volume simulated, which covers a Box with a side length of 2688Mpc $h^{-1}$, simulated using $2 \times 4536^3$ particles (for details, see Bocquet et al. 2016). We adopted a *WMAP7* (Komatsu et al. 2011) ΛCDM cosmology with $\sigma_8 = 0.809$, $h = 0.704$, $\Omega_\Lambda = 0.728$, $\Omega_m = 0.272$, $\Omega_b = 0.0456$, and an initial slope for the power spectrum of $n_s = 0.963$.

The simulation is based on the parallel cosmological Tree Particle-Mesh smoothed-particle hydrodynamics (SPH) code P-GADGET3 (Springel 2005). The code uses an entropy-conserving formulation of SPH (Springel & Hernquist 2002) and follows the gas using a low-viscosity SPH scheme to properly track turbulence (Dolag et al. 2005). Based on Dolag et al. (2004), it also follows thermal conduction at 1/20th of the classical *Spitzer* value (Spitzer 1962) and allows a treatment of radiative cooling, heating from a uniform time-dependent ultraviolet background and star formation with the associated feedback processes.

We model the interstellar medium (ISM) by using a sub-resolution model for the multiphase ISM of Springel & Hernquist (2003). In this model, the ISM is treated as a two-phase medium, in which clouds of cold gas form by cooling of hot gas, and are embedded in the hot gas phase assuming pressure equilibrium whenever gas particles are above a given threshold density. The hot gas within the multiphase model is heated by supernovae and can evaporate the cold clouds. A certain fraction of massive stars (10 per cent) is assumed to explode as supernovae Type II (SNII). The released energy by SNII ($10^{51}$ erg) triggers galactic winds with a mass loading rate proportional to the star formation rate with a resulting wind velocity of $v_{wind} = 350$ km $s^{-1}$. Radiative cooling rates are computed by following the same procedure presented by Wiersma, Schaye & Smith (2009) and include a detailed model of chemical evolution according to Tornatore et al. (2007). Metals are produced by SNII, by supernovae Type Ia (SNIa) and by intermediate and low-mass stars in the asymptotic giant branch. Metals and energy are released by stars of different masses, initially distributed according to a Chabrier initial mass function (IMF; Chabrier 2003).

Most importantly, *Magneticum Pathfinder* simulations include prescriptions for the growth of black holes and the feedback from AGNs based on the model of Springel, Di Matteo & Hernquist (2005) and Di Matteo, Springel & Hernquist (2005). Here, the accretion on to black holes and the associated feedback adopt a sub-resolution model. Black holes are represented by collisionless 'sink particles', which can grow in mass by either accreting gas from their environments or merging with other black holes. The radiated luminosity of the AGN in this model is related to the black hole accretion. In addition, we incorporate the feedback prescription of Fabjan et al. (2010); namely, we account for a transition from a quasar- to a radio-mode feedback whenever the accretion rate $\dot{M}_{BH}$ (where $M_{BH}$ is the black hole mass) is low. We introduced some more technical modifications of the original implementation, for which readers can find details in Hirschmann et al. (2014), where we also demonstrate that the bulk properties of the AGN population within the simulation are quite similar to the observed AGN properties.

We use the SUBFIND algorithm (Springel et al. 2001; Dolag et al. 2009) to define halo and sub-halo properties. SUBFIND identifies sub-structures as locally overdense, gravitationally bound groups of particles. Starting with a main halo identified through the Friends-of-Friends (FoF) algorithm with a linking length of 0.16 times the mean interparticle separation, a local density is estimated for each particle via adaptive kernel estimation, using a prescribed number of smoothing neighbours. Starting from isolated density peaks, additional particles are added in sequence of decreasing density. Whenever a saddle point in the global density field is reached that connects two disjoint overdense regions, the smaller structure is treated as a sub-structure candidate, and the two regions are then merged. All sub-structure candidates are subject to an iterative unbinding procedure with a tree-based calculation of the potential. These structures can then be associated with galaxies, and their integrated properties (such as stellar mass, $M_*$) can then be calculated. For the main haloes identified by the FoF algorithm, the virial radius is calculated using a density contrast based on the top-hat model (Eke, Cole & Frenk 1996). For comparison with observations, we additionally use overdensity with respect to 500 times the critical density to define $M_{500c}$, which is the mass we will refer to as cluster mass in this paper. We refer to clusters as main haloes with $M_{500c} > 10^{13}\,M_\odot\,h^{-1}$.

For our analysis we make use of the galaxy, cluster and AGN samples extracted from the simulation at redshift $z = 0.14$ with the criteria explained above. In Table 1 we summarize some properties of the samples which are relevant for our work.

**Table 1.** Properties of the galaxy, cluster and AGN populations extracted from the *Magneticum* simulations. We report the minimum mass of the object included, $M_{min}$, in terms of stellar masses $M_*$ for the galaxies, $M_{500c}$ for clusters and $M_{BH}$ for AGNs, as well as the number of tracers $N_t$ and of identified voids $N_v$.

| Tracers | $M_{min}[M_\odot\,h^{-1}]$ | $N_t$ | $N_v$ |
|---|---|---|---|
| Galaxies | $M_* = 4 \times 10^8$ | $9.5 \times 10^6$ | 36 430 |
| Clusters | $M_{500c} = 1 \times 10^{13}$ | $2.6 \times 10^6$ | 16 970 |
| | $M_{500c} = 5 \times 10^{13}$ | $3.5 \times 10^5$ | 3125 |
| | $M_{500c} = 1 \times 10^{14}$ | $1.0 \times 10^5$ | 1053 |
| AGNs | $M_{BH} = 4 \times 10^6$ | $5.3 \times 10^6$ | 26 265 |

[1] See http://www.magneticum.org.

## 3 METHODOLOGY

In this section we will briefly recap how the tracer bias is defined in observations and theory. We will also present the void finder we used and summarize some properties of void profiles that are relevant for this work.

### 3.1 Correlation functions and bias estimation

The tracer correlation function is a measure of the degree of clustering of the tracer itself. Being $\mathrm{d}^2P$ the probability that a tracer $A$ in the volume $\mathrm{d}V_A$ and another tracer $B$ in the volume $\mathrm{d}V_B$ are separated by a distance $r$, the spatial two-point correlation function, $\xi_{AB}(r)$, is defined as the deviation of such probability from that expected from a random distribution of tracers:

$$\mathrm{d}^2P = \langle n_A\rangle\langle n_B\rangle[1+\xi_{AB}(r)]\mathrm{d}V_A\mathrm{d}V_B \tag{1}$$

where $\langle n_A\rangle$ and $\langle n_B\rangle$ are the mean densities of the tracers (Peebles 1980). When we compare tracers of the same population, we refer to $\xi$ as the auto-correlation function while, if we compare two kinds of tracers, we refer to $\xi$ as cross-correlation function.

In general, there is no reason to assume that the distribution of baryons in the Universe traces exactly the distribution of mass. In fact, on small scales, galaxy formation involves many dissipative processes such as the radiative cooling of hot gas, so the efficiency of galaxy formation is related to how deep the potential wells created by haloes were; hence, on small scales, bias between matter and tracers is a complicated function of space and time. By looking at the distribution of tracers on very large scales, we can only observe the most luminous galaxies which are hosted by the most massive haloes (Kaiser 1984), i.e. by the highest peaks in the density field. Thereby, in the latter regime, tracers still do not perfectly mirror the same distribution as matter, but, since the density fluctuations are small, the relation between matter and luminous tracers results in a constant offset in the clustering amplitude, the *linear bias*, which, in terms of spatial correlations, can be written as:

$$b = \xi_{\mathrm{tm}}/\xi_{\mathrm{mm}}, \tag{2}$$

or

$$b = \sqrt{\xi_{\mathrm{tt}}/\xi_{\mathrm{mm}}}, \tag{3}$$

where $\xi_{\mathrm{tm}}$ is the tracer–matter cross-correlation function, $\xi_{\mathrm{mm}}$ is the matter auto-correlation function and $\xi_{\mathrm{tt}}$ is the tracer auto-correlation function (the tracers being galaxies, clusters and AGNs for our purposes). We make use of these two definitions to calculate the value of the linear bias of tracers in the *Magneticum* simulation.

### 3.2 Theoretical bias

The excursion set formalism, introduced by Press & Schechter (1974) to predict the number of virialized dark matter haloes in the Universe and fully developed by Bond et al. (1991), provides a neat framework to develop a simple theoretical model to calculate the clustering of dark matter haloes and how their spatial distribution is biased with respect to that of the mass. With this approach, Mo & White (1996) estimated the bias, $b_{\mathrm{MW}}$, as

$$b_{\mathrm{MW}} = 1 + \frac{\nu^2-1}{\delta_{\mathrm{crit}}}, \tag{4}$$

where $\delta_{\mathrm{crit}}$ is the critical density exceeding which the collapse occurs and $\nu \equiv \delta_{\mathrm{crit}}/\sigma(M)$ is the height of the threshold in units of the variance of the smoothed density distribution, $\sigma(M)$, at a given halo mass, $M$:

$$\sigma^2(M) = \frac{1}{2\pi}\int_0^\infty \mathrm{d}k k^2 P_{\mathrm{m}}(k,z)\tilde{W}_R^2(k), \tag{5}$$

$P_{\mathrm{m}}(k,z)$ being the matter power spectrum at redshift $z$ and $\tilde{W}_R(k)$ the Fourier transform of the top-hat filter function (for a review of these topics, we refer to Zentner 2007).

However, the bias as expressed by equation (4) fails to predict with high accuracy the value of the bias measured in numerical simulations. For this reason, various corrections to equation (4) have been proposed to improve the consistency with simulation results (see e.g. Sheth & Tormen 1999, 2002; Sheth, Mo & Tormen 2001; Seljak & Warren 2004; Tinker et al. 2010). In particular, Tinker et al. (2010) show how, by calibration with a large set of simulations, it is possible to estimate bias to great accuracy. Following the results of Tinker et al. (2010), the linear bias $b_{\mathrm{Tinker}}$ reads as:

$$b_{\mathrm{Tinker}} = 1 - A\frac{\nu^a}{\nu^a+\delta_{\mathrm{crit}}^a} + B\nu^b + C\nu^c, \tag{6}$$

where $a$, $A$, $b$, $B$, $c$, $C$ are the calibrated parameters.

We will compute the theoretical value of the linear bias in the *Magneticum simulations* using both the formula by Mo&White and its correction by Tinker. In order to calculate the theoretical mean value of the bias associated with our cluster sample, we will average its value using the number of objects as a function of their mass (the cluster mass function) $\frac{\mathrm{d}n}{\mathrm{d}M}$, i.e.

$$\langle b\rangle = \frac{1}{\langle n_{\mathrm{t}}\rangle}\int_{M_{\mathrm{min}}}^{M_{\mathrm{max}}}\frac{\mathrm{d}n}{\mathrm{d}M}b(M)\mathrm{d}M, \tag{7}$$

where $M_{\mathrm{min}}$ and $M_{\mathrm{max}}$ are the lowest and largest masses in the sample, respectively.

### 3.3 The void finder

The biggest criticism concerning void studies is generally related to the ambiguity of the void definition: there are in fact many different available finders and, in some circumstances, the usage of such a variety of recipes to identify voids can lead to results almost impossible to compare (Colberg et al. 2008). Although the void definition can be a serious obstacle on the way to establish a coherent picture on void properties, previous works proved that some statistical properties of voids (such as their number function or profile) are strongly affected by galaxy bias independently of the finder in use. In particular, recent papers exploiting the differences between voids in a ΛCDM cosmology and modifications of gravity (Cai et al. 2015), Galileon or non-local gravity (Barreira et al. 2015), or possible couplings between CDM and DE (Pollina et al. 2016) conclude that, while voids identified by matter particles exhibit a clear deviation from the ΛCDM case, it is impossible to discriminate between models looking at the statistics of voids identified by haloes. While Barreira et al. (2015) connect the latter result with the poor statistic of the halo-sample, Cai et al. (2015) suggest that this feature is related to the halo bias in agreement with Pollina et al. (2016), where the authors verified that the poor statistic of haloes is not sufficient to justify the dissimilar properties displayed by voids in haloes and voids in matter. A similar conclusion has been drawn independently by Nadathur & Hotchkiss (2015a) using a ΛCDM simulation. It is a quite remarkable fact that all of these works reach the same conclusion using different void-finders, namely, an improved version of the finder presented in Padilla et al. 2005 (employed by Cai et al. 2015), the Watershed Void Finder algorithm (Platen, van de

Weygaert & Jones 2007b, used by Barreira et al. 2015), VIDE (Sutter et al. 2015, utilized by Pollina et al. 2016) and a modified version of ZOBOV (Neyrinck 2008, employed by Nadathur & Hotchkiss 2015a). So, although it has been pointed out that a dynamical approach in void finding (in which there is no reliance on particle positions) can reduce the impact of shot noise in void identification (see e.g. Elyiv et al. 2015), this is not relevant for this study where we look directly at bias effects, which, as clarified above, are visible independently of the finder in use. That said, it is crucial to be as clear as possible in the description of the void finder and of a possible selection applied on top of the void catalogue to ensure that conclusions and results attained are plausible and can be reproduced by other parties. In the following lines we present the finder we employed for our analysis.

We make use of the publicly available void finder VIDE (Void IDentification and Examination toolkit; Sutter et al. 2015) to identify voids. VIDE is a wrapper for ZOBOV (ZOnes Bordering On Voidness; Neyrinck 2008), an algorithm that identifies depressions in the density distribution of a set of points and merges them in voids with a watershed transform. Here we provide a summary of how ZOBOV works, outlining the basic points of the procedure, and we refer the interested readers to the original ZOBOV paper (Neyrinck 2008) and to the VIDE paper (Sutter et al. 2015) for a more detailed discussion.

The void-finding technique in ZOBOV has four fundamental steps.

(i) *Voronoi tessellation* – a cell is associated with each particle $p$ following the prescription that a cell associated with $p$ is the region of the box which is closer to $p$ than to any other particle in the box. The reciprocal of the cell volume is an estimate of its density. Hence, with this first step we define the density field in which to look for voids.

(ii) *Definition of density minima* – the algorithm finds minima in the density field established in step (*i*). A density minimum is defined as a Voronoi cell with a density lower than all its adjacent cells.

(iii) *Creation of basins* – ZOBOV joins together cells of increasing density surrounding a density minimum until no adjacent higher-density cell is found; this defines *basins* as the union of these cells. Basins are depressions in the density field, i.e. they could be considered as voids themselves, but single basins may also arise from spurious Poisson fluctuations due to particle discreteness.

(iv) *Watershed transform* – basins are joined together using a watershed algorithm (see Platen et al. 2007b) to form larger voids under the condition that the ridge between basins has a density lower than a given threshold (which is set to be the 20 per cent of the mean density of the universe within the VIDE framework). This technique naturally builds up a hierarchy in the structure of voids, including sub-voids.

These steps are implemented by the enhanced version of the ZOBOV algorithm included in the VIDE toolkit. Additionally, VIDE calculates the void centre as the volume-weighted barycentre, $\boldsymbol{x}^c$, of the cells included in a void:

$$\boldsymbol{x}^c = \frac{\sum_{i=1}^{N} \boldsymbol{x}_i^t \cdot V_i^t}{\sum_{i=1}^{N} V_i^t}, \tag{8}$$

where $\boldsymbol{x}_i^t$ and $V_i^t$ are the positions of the $i$th tracer (i.e. particle) $t$ and the volume of its associated Voronoi cell, respectively, and $N$ is the number of particles included in the void. The effective radius of the void, $R_{\rm eff}$, is computed from the overall volume of the underdense region by assuming sphericity:

$$V_{\rm void} \equiv \sum_{i=1}^{N} V_i^t = \frac{4}{3}\pi R_{\rm eff}^3. \tag{9}$$

VIDE provides many catalogues in which various types of sample selections (as e.g. cuts on the void hierarchy or on the void central density) are applied on top of the original ZOBOV sample. Since for observations it is often undesirable to perform a selection on the void sample due to poor statistics, we will apply no selection regarding void hierarchy or central density, thereby allowing also voids-in-clouds (voids in overdense environment) in our analysis.

The ZOBOV code was originally intended for void finding in simulations, but VIDE also provides a flag for void identification in light cones from observations including the survey mask into the analysis (see the VIDE paper Sutter et al. 2015, for further information) and, in fact, several catalogues of voids in spectroscopic samples are already available (Pan et al. 2012; Sutter et al. 2012a; Ceccarelli et al. 2013; Nadathur 2016; Mao et al. 2017). Computationally we therefore have no problem in handling void finding in observations. The issue left to address is how to incorporate the bias into our framework, since we will need to relate properties of voids identified in the distribution of luminous tracers of the dark matter with voids in the dark matter distribution itself, that are usually under study in simulations. We will elucidate this relation in the following sections of this paper.

### 3.4 Density profile of cosmic voids

The void density profile is one of the basic void statistics. From previous studies it is known that the spherically averaged profile of voids exhibits a very simple structure (see e.g. Hamaus et al. 2014c; Ricciardelli et al. 2013, 2014): voids are deeply underdense in the vicinity of their centre and feature an overdense compensation wall at $r \approx R_{\rm eff}$, where $r$ is the radial distance from the void centre. Such a density profile can be described with a simple fitting formula (Hamaus et al. 2014c):

$$\frac{n_{\rm vt}}{\langle n_{\rm t}\rangle} - 1 = \delta_{\rm c}\frac{1-(r/r_{\rm s})^{\alpha}}{1+(r/R_{\rm eff})^{\beta}}, \tag{10}$$

where $\delta_{\rm c}$ is the central density contrast, $r_{\rm s}$ is a scale radius at which the profile density, $n_{\rm vt}$, is equal to the average density of tracer $\langle n_{\rm t}\rangle$ and $\alpha$ and $\beta$ describe the inner and outer slopes of the void profile.

It is possible to show that the density profile of voids encodes the same information as the void–tracer cross-correlation function. In fact, the radial profile of voids is nothing but a procedure by means of which we count tracers at a given distance from the void centre per units of volume, i.e. the cross-correlation between centres and tracers by definition (see e.g. Hamaus et al. 2015). Calling $N_{\rm t}$ the number of tracers, $N_{\rm v}$ the number of voids, $\delta^{\rm D}$ Dirac's delta function, $V$ the total volume, $\boldsymbol{x}_i^{\rm c}$ the coordinates of the centre of the $i$th void and $\boldsymbol{x}_j^t$ the coordinates of the $j$th tracer we can show explicitly that the radial spherically averaged void tracer-density profile compared to the mean tracer density of the Universe is:

$$\begin{aligned}\frac{n_{\rm vt}(r)}{\langle n_{\rm t}\rangle} &= \frac{1}{N_{\rm v}}\sum_i \frac{n_{\rm vt}^i(r)}{\langle n_{\rm t}\rangle} = \frac{1}{N_{\rm v}}\sum_i \frac{1}{N_{\rm t}} V \sum_j \delta^D\left(\boldsymbol{x}_i^c - \boldsymbol{x}_j^t + \boldsymbol{r}\right)\\ &= V\sum_{i,j}\int \frac{1}{N_{\rm v}}\delta^D\left(\boldsymbol{x}_i^c - \boldsymbol{x}\right)\frac{1}{N_{\rm t}}\delta^D(\boldsymbol{x} - \boldsymbol{x}_j^t + \boldsymbol{r})d^3x\\ &= \frac{1}{V}\int \frac{n_{\rm v}(\boldsymbol{x})}{\langle n_{\rm v}\rangle}\frac{n_{\rm t}(\boldsymbol{x}+\boldsymbol{r})}{\langle n_{\rm t}\rangle}d^3x = 1 + \xi_{\rm vt}(r)\end{aligned}$$

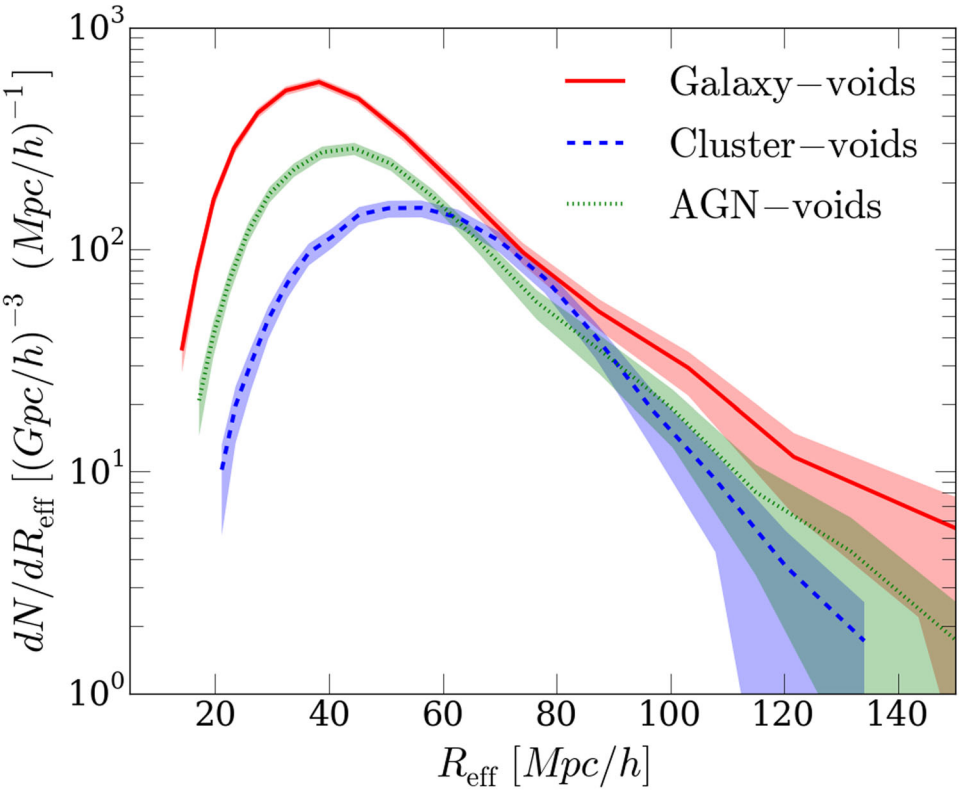


**Figure 1.** Abundances of voids in the *Magneticum* simulation. Voids are identified in the distribution of galaxies (solid red line), clusters (dashed blue line) and AGN (dotted green line). The shaded area represents the error, calculated as Poisson uncertainty on the number counts. Using galaxies as tracers of the underlying density field of the Universe, we are able to resolve and find a sample of voids with a typical size between 15 and 60 Mpc $h^{-1}$, twice as many as the sample of AGN voids and four times as many as cluster voids in the same range of size. We expect such a result due to the effect of the tracer sparsity on void finding (see Sutter et al. 2014b): with a low number of tracers (see Table 1), we are not able to resolve voids of small size.

thereby proving that

$$\frac{n_{\rm vt}(r)}{\langle n_{\rm t}\rangle} - 1 = \xi_{\rm vt}(r), \tag{11}$$

as we wanted to show.

## 4 THE STATISTICS OF VOIDS IN THE *MAGNETICUM PATHFINDER* SIMULATIONS

The aim of this work is to study the distribution of matter around potentially observable voids, i.e. voids identified in the distribution of luminous tracers, such as galaxies, clusters or AGNs. The basic idea is to run our void-finder (described in Section 3.3) on the galaxy, cluster and AGN catalogues extracted from a large fully-hydro simulation (the *Magneticum*; see Section 2) and calculate both the density-profile of dark matter and of its tracers around voids. A similar study has been conducted by Sutter et al. (2014a), although the main purpose there was to show that voids in galaxies coincide with underdense regions of the dark matter distribution, which is indeed a crucial study to investigate potentially observable properties of voids. The authors also perform a void-to-void comparison for voids identified by galaxies and by matter particles. They conclude that it is always possible to identify a matter void in the vicinity of a galaxy void, although an offset between their centres is usually present. At that stage it has been concluded that potentially observable voids are indicative of the presence of an underdensity of matter in our Universe. As we have now evidence that the tracer bias is playing a fundamental role in void-analysis (see the discussion at the beginning of Section 3.3), we need to further investigate the relation between tracers and the matter distribution around voids, which is the goal of the present work.

In the following, we will refer to galaxy voids, cluster voids or AGN voids to indicate voids which are defined by applying the finder on the galaxy sample, the cluster sample or the AGN sample. More generally, we will refer to tracer-voids to indicate the three of them at the same time.

### 4.1 Dark matter distribution around void centres

To have a first overview of the void catalogues we are about to use, we look at the size distribution of voids, which is displayed in Fig. 1. This figure shows the number of voids as a function of $R_{\rm eff}$. Voids in *Magneticum* have sizes between 15 and 150 Mpc $h^{-1}$ (we refer to the largest volume simulated, where the box-size is 2688 Mpc $h^{-1}$). As we could have expected due to the number of tracers available in each sample (see Table 1) and its effect on void finding (see Sutter et al. 2014b), we resolve the smallest voids in the galaxy sample, where we see twice as many voids of size within 15–60 Mpc $h^{-1}$ as in the AGN sample and four times as many as in the cluster sample.

After this preliminary check, we can look at the distribution of matter around void centres identified by the tracers. In the top panel of Fig. 2, we show the stacked density profiles (i.e. the average density profile of voids of similar size) for tracer-voids with 80 Mpc $h^{-1}$ < $R_{\rm eff}$ < 90 Mpc $h^{-1}$ (the tracers being galaxies, clusters and AGNs from the left to the right). Each profile is calculated by counting objects (tracers or dark matter particles) in the volume

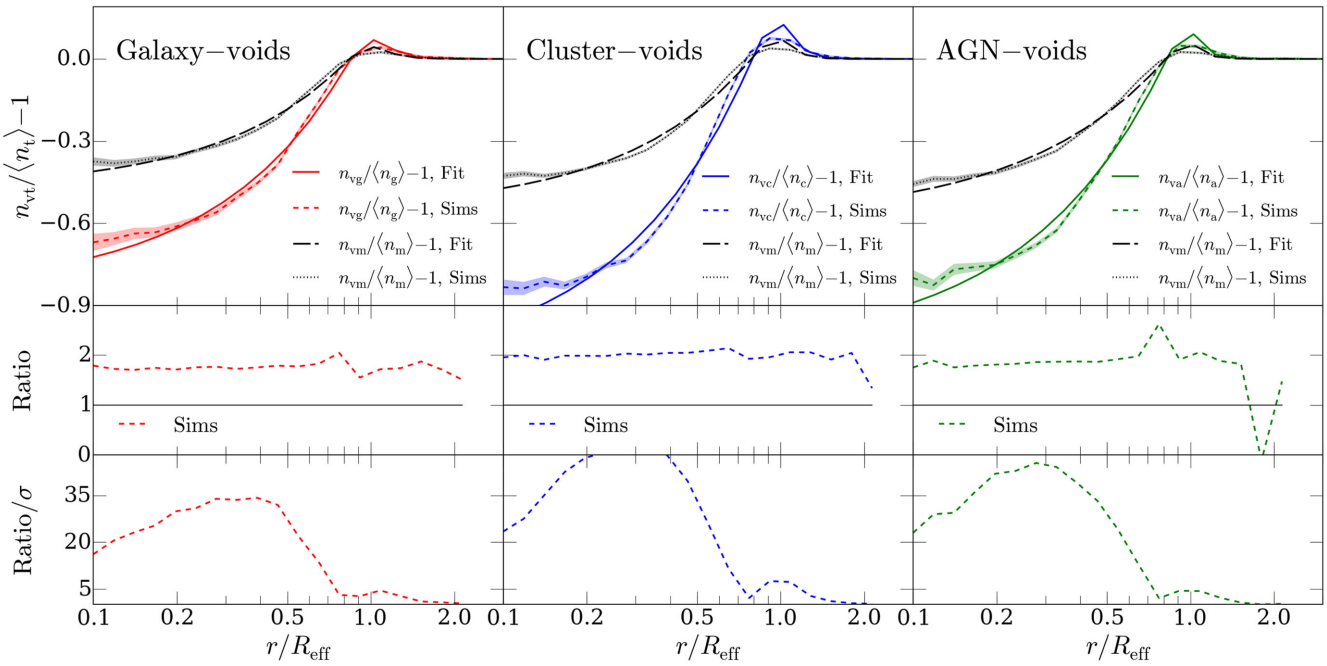


**Figure 2.** Top panels: measured overdensity of tracers (short dashed line) and of matter (dotted line) around tracer-void centres (tracers being galaxies, clusters and AGNs from the left to the right). The solid lines show the fit of the tracer profile using equation (10). The same formula can be used to fit the matter profiles (long dashed lines). The shaded areas are the uncertainty computed as the standard deviation from the mean profiles. In the mid-panels we plot the ratios between tracer profiles and matter profiles around tracer-void centres, which look fairly constant. In the bottom panels we display the signal-to-noise ratios of the mid-panels. As the values of the measured profiles encounter zero, the signal-to-noise ratio drops dramatically. These profiles are obtained by stacking voids with $80\,{\rm Mpc\,h^{-1}} < R_{\rm eff} < 90\,{\rm Mpc\,h^{-1}}$.

of spherical shells; the distances from void centres are expressed in units of $R_{\rm eff}$ and the profile density, $n_{\rm vt}$, is expressed in terms of the mean density of tracers in the Universe $\langle n_{\rm t}\rangle$. The errors are calculated as the standard deviation from the average density profile. We use full catalogues (for matter and tracers) without applying any sub-sampling in order to reduce as much as possible the impact of noise caused by sparsity. In the top panels of Fig. 2, the short dashed lines show the measured tracer-density profiles of tracer-voids in *Magneticum* simulations and the solid lines are their fits computed with the formula given in equation (10): as expected the fitting formula correctly describes the tracers' distribution around tracer-voids (Sutter et al. 2014b). The dotted lines represent the matter distribution around tracer-void centres, and the long-dashed lines are their fits again with equation (10). The formula by Hamaus et al. (2014c) correctly describes the matter distribution around voids defined in tracers too. The discrepancy in the inner regions is due to some residual sparsity effect, which becomes more important in the vicinity of void centres. The fact that equation (10) correctly describes also the dark matter underdensities around tracer-voids is a first interesting result; in fact, although equation (10) has been already successfully tested on both matter voids and galaxy voids separately, in this particular case we are not defining voids in the matter itself: the void-finder is run only on top of observable tracers and we then look at the matter distribution around these potentially observable voids. So the profiles of voids are always self-similar and describable by equation (10) although the finder is not directly run on the particles with which the profile is computed. Furthermore, in principle, once a relation between the tracer-density profile and the matter-density profile is established, we can link the latter to a potentially observable void-profile, therefore opening up the possibility of testing this finding with observations of voids where we can use the relative bias between tracers to calibrate this feature. Going back to the top panels of Fig. 2, we observe that, as expected from theory and previous works (Sutter et al. 2014a), the tracer distributions around tracer-voids show a steeper profile when compared to the matter: in the vicinity of the void centres, we measure a larger matter density than tracer density, while on the edge of voids (i.e. around $r \approx R_{\rm eff}$) the tracer density is higher than the matter density.

In the middle panels of Fig. 2, we display the ratio between the measured matter profiles and tracer profiles (dashed line). Although all ratios look fairly constant, there is a large signal-to-noise ratio drop at $r \approx 0.75R_{\rm eff}$, i.e. where profiles have overdensities close to zero. This is shown clearly in the bottom panels of Fig. 2, in which the signal-to-noise ratio (where the noise is computed using error propagation, starting with the error on the density profiles) for the mid-panels is displayed. The fact that the ratios between tracer profiles and matter profiles look fairly constant is very promising, but it can be too naive to trust the values given by the profile ratios as indicators of the matter–tracer relation considering the large signal-to-noise ratio drop just discussed.

Another way to look at the dependence between matter and tracer distributions around voids is to plot one as function of the other. In Fig. 3 we show the matter distribution around tracer-voids as a function of tracer distributions where the measured points are displayed as points with error bars in both directions. We can fit these points with a simple linear function (dotted line):

$$\frac{n_{\rm vt}}{\langle n_{\rm t}\rangle} - 1 = b_{\rm slope}\left(\frac{n_{\rm vm}}{\langle n_{\rm m}\rangle} - 1\right) + c_{\rm offset}, \tag{12}$$

where $n_{\rm vt}$ is the measured tracer-density profile around tracer-voids, $\langle n_{\rm t}\rangle$ is the mean tracer density, $n_{\rm vm}$ is the measured matter-density profile around tracer-voids, $\langle n_{\rm m}\rangle$ is the mean matter density of the

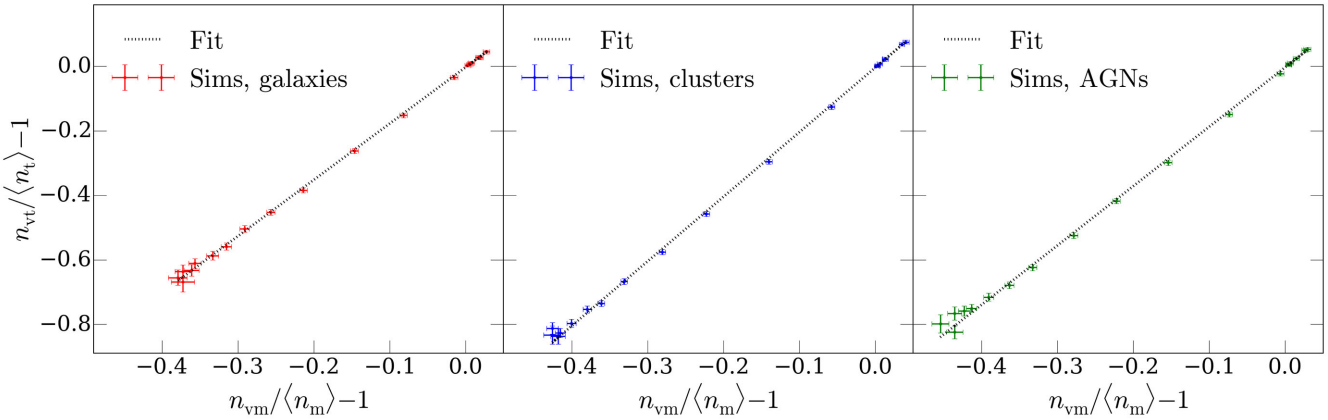


**Figure 3.** Overdensity of luminous tracers around voids as a function of the matter overdensity around tracer-void centres (both taken from Fig. 2). The measured points are fitted with the linear function (dotted line) from equation (12), in which the offset is consistent to zero within 5 per cent (see Table 2). The error bars show the standard deviation from the mean profiles. From left to right the tracers are galaxies, clusters and AGNs.

**Table 2.** Values of fit parameters in equation (12) for each tracer and void size. We do not resolve enough cluster voids with $20\,{\rm Mpc\,h^{-1}} < R_{\rm eff} < 30\,{\rm Mpc\,h^{-1}}$ to perform our analysis, hence we cannot report the values of the parameters in that case.

| Voids | Galaxies | | Clusters ($M_{500c} \geq 10^{13}{\rm M}_\odot\,h^{-1}$) | | AGNs | |
|---|---|---|---|---|---|---|
| Bin in void size | $b_{\rm slope}$ | $c_{\rm offset}$ | $b_{\rm slope}$ | $c_{\rm offset}$ | $b_{\rm slope}$ | $c_{\rm offset}$ |
| $20\,{\rm Mpc\,h^{-1}} < R_{\rm eff} < 30\,{\rm Mpc\,h^{-1}}$ | $2.164 \pm 0.061$ | $-0.098 \pm 0.012$ | – | – | $2.395 \pm 0.107$ | $-0.086 \pm 0.020$ |
| $30\,{\rm Mpc\,h^{-1}} < R_{\rm eff} < 40\,{\rm Mpc\,h^{-1}}$ | $2.046 \pm 0.026$ | $-0.057 \pm 0.004$ | $2.415 \pm 0.046$ | $-0.041 \pm 0.005$ | $2.305 \pm 0.052$ | $-0.070 \pm 0.007$ |
| $40\,{\rm Mpc\,h^{-1}} < R_{\rm eff} < 50\,{\rm Mpc\,h^{-1}}$ | $1.890 \pm 0.014$ | $-0.023 \pm 0.003$ | $2.259 \pm 0.027$ | $-0.020 \pm 0.003$ | $2.125 \pm 0.026$ | $-0.030 \pm 0.004$ |
| $50\,{\rm Mpc\,h^{-1}} < R_{\rm eff} < 60\,{\rm Mpc\,h^{-1}}$ | $1.800 \pm 0.012$ | $-0.011 \pm 0.003$ | $2.144 \pm 0.016$ | $-0.011 \pm 0.002$ | $2.006 \pm 0.021$ | $-0.021 \pm 0.003$ |
| $60\,{\rm Mpc\,h^{-1}} < R_{\rm eff} < 70\,{\rm Mpc\,h^{-1}}$ | $1.751 \pm 0.011$ | $-0.007 \pm 0.002$ | $2.089 \pm 0.011$ | $-0.007 \pm 0.001$ | $1.925 \pm 0.014$ | $-0.007 \pm 0.002$ |
| $70\,{\rm Mpc\,h^{-1}} < R_{\rm eff} < 80\,{\rm Mpc\,h^{-1}}$ | $1.738 \pm 0.008$ | $-0.005 \pm 0.002$ | $2.030 \pm 0.010$ | $-0.005 \pm 0.001$ | $1.875 \pm 0.012$ | $-0.006 \pm 0.002$ |
| $80\,{\rm Mpc\,h^{-1}} < R_{\rm eff} < 90\,{\rm Mpc\,h^{-1}}$ | $1.746 \pm 0.006$ | $-0.004 \pm 0.001$ | $2.001 \pm 0.010$ | $-0.004 \pm 0.001$ | $1.840 \pm 0.011$ | $-0.005 \pm 0.001$ |
| $90\,{\rm Mpc\,h^{-1}} < R_{\rm eff} < 100\,{\rm Mpc\,h^{-1}}$ | $1.725 \pm 0.008$ | $-0.003 \pm 0.001$ | $1.972 \pm 0.015$ | $-0.003 \pm 0.002$ | $1.841 \pm 0.010$ | $-0.004 \pm 0.001$ |
| $100\,{\rm Mpc\,h^{-1}} < R_{\rm eff} < 110\,{\rm Mpc\,h^{-1}}$ | $1.767 \pm 0.010$ | $-0.002 \pm 0.001$ | $1.953 \pm 0.014$ | $-0.001 \pm 0.002$ | $1.852 \pm 0.014$ | $-0.002 \pm 0.001$ |
| $110\,{\rm Mpc\,h^{-1}} < R_{\rm eff} < 120\,{\rm Mpc\,h^{-1}}$ | $1.751 \pm 0.007$ | $-0.002 \pm 0.001$ | $1.908 \pm 0.017$ | $-0.003 \pm 0.002$ | $1.862 \pm 0.022$ | $-0.001 \pm 0.002$ |
| $120\,{\rm Mpc\,h^{-1}} < R_{\rm eff} < 130\,{\rm Mpc\,h^{-1}}$ | $1.735 \pm 0.021$ | $-0.002 \pm 0.001$ | $1.958 \pm 0.019$ | $-0.003 \pm 0.002$ | $1.892 \pm 0.020$ | $-0.001 \pm 0.001$ |
| $130\,{\rm Mpc\,h^{-1}} < R_{\rm eff} < 150\,{\rm Mpc\,h^{-1}}$ | $1.764 \pm 0.012$ | $-0.004 \pm 0.001$ | $1.951 \pm 0.065$ | $-0.007 \pm 0.008$ | $1.869 \pm 0.021$ | $-0.004 \pm 0.002$ |

Universe and $b_{\rm slope}$ and $c_{\rm offset}$ are the two free parameters of the linear fit, i.e. the slope and the offset, respectively. We find that the value of $c_{\rm offset}$ is always consistent with zero within 5 per cent (except, due to sparsity, for small voids with $20\,{\rm Mpc\,h^{-1}} < R_{\rm eff} < 30\,{\rm Mpc\,h^{-1}}$, in which $c_{\rm offset} \approx 0$ only within the 10 per cent; see Table 2). Therefore, $b_{\rm slope}$ provides a single value which fully describes the relation between matter and tracer distributions: hence, we expect $b_{\rm slope}$ to be related to the linear bias. In the following we will show that $b_{\rm slope}$ in fact coincides with the linear bias, if sufficiently large voids are considered. This result suggests two main consequences: not only can we link the tracer profiles and matter profile of voids using the linear bias, but we can also think of $b_{\rm slope}$ as a novel way to measure the bias. We will discuss this latter possibility in Section 4.2.

What we have shown so far refers to voids with an effective radius $R_{\rm eff}$ within 80 and 90 $\,{\rm Mpc\,h^{-1}}$ as a guiding example, but we did perform our analysis using voids of various sizes. We report the bins in which the analysis is repeated in the first column of Table 2. The bins are selected such that:

(i) a sufficient number of voids are included in each bin so that the averaged profile is accurate enough to make the profile-fit and the linear-fit converge (i.e. at least ≈50 voids per bin);

(ii) the physical dimension of each single bin is not too extended, in order to work under the hypothesis of considering voids of similar sizes, which is required by equation (10);

(iii) all void sizes are covered.

We verified that in each bin we can always fit the relation between matter and tracers around voids with a simple linear relation. In Fig. 4, we show the values for $b_{\rm slope}$ (see equation 12) as a function of void size (the tracers being, from the left, galaxies, clusters and AGNs). We see a trend: the value of $b_{\rm slope}$ decreases with the increase of void size, showing that small voids yield a larger bias. As the size of voids surpasses a critical size, the value of $b_{\rm slope}$ stabilizes asymptotically to a constant value. The critical void size at which $b_{\rm slope}$ becomes stable seems to be dependent on the tracer properties (clusters, mid-panel, seem stable only starting at $R_{\rm eff} \approx 80\,{\rm Mpc\,h^{-1}}$, while galaxies and AGNs show a stable value of $b_{\rm slope}$ for roughly $R_{\rm eff} > 50\,{\rm Mpc\,h^{-1}}$) and on the number of tracers (i.e. on the sparsity of the sample). The shaded areas in Fig. 4 represent the uncertainty obtained from the linear fits.

### 4.2 Linear bias

To demonstrate convincingly that $b_{\rm slope}$ from our fit with equation (12) is an indicator of the tracer bias, we compare its values with the most commonly used bias estimators (discussed in Section 3.2). In Fig. 5 we show the bias computed with equations (2) (dashed lines) and (3) (dotted lines) and $b^l_{\rm slope}$ (solid lines), defined as the value of $b_{\rm slope}$ calculated in the bin that includes the largest voids of

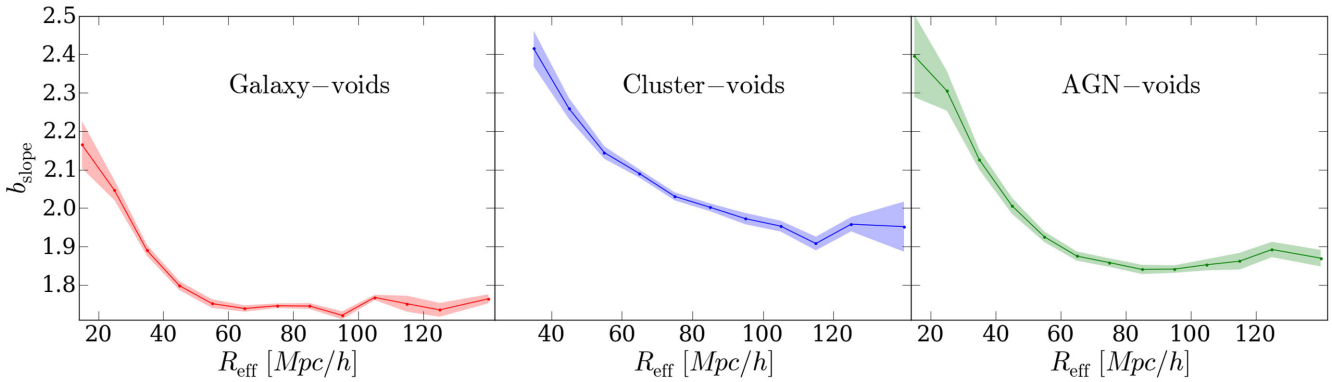


**Figure 4.** Value of $b_{\rm slope}$ from Fig. 3 for galaxies (left-hand panel), clusters (mid-panel) and AGNs (right-hand panel) around galaxy voids, cluster voids and AGN voids, respectively, in various void-radius bins (i.e. as a function of void size). The shaded area represents the uncertainty, obtained from the error on the fit. We see an impact of void size on the measurement of $b_{\rm slope}$, which becomes larger for small voids.

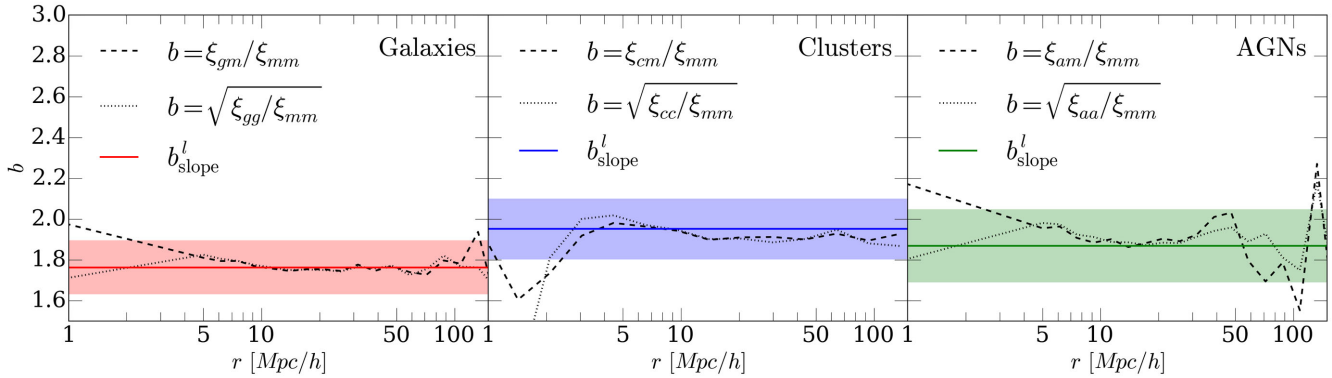


**Figure 5.** Comparison between different bias estimators: starting from the left-hand panel, we plot the bias of galaxies calculated as the saturated value of the slopes from Fig. 4, and the usual galaxy bias estimators presented in equation (2) (dashed line) and equation (3) (dotted line). The central and right-hand panels show the cases of clusters and AGNs in blue and green, respectively. We find a good consistency between $b^l_{\rm slope}$ and other bias estimators in the large-scale limit. The shaded area is the error, computed as the standard deviation from the mean value of $b_{\rm slope}$ from all void sizes.

each sample (i.e. 130 Mpc h$^{-1}$ < $R_{\rm eff}$ < 150 Mpc h$^{-1}$): the aim is to confront the asymptotic measured value of $b_{\rm slope}$ (see Fig. 4) with the linear bias. The shaded areas show the error on the mean value of $b_{\rm slope}$ from all void sizes.

As we can see in Fig. 5, for all tracers (from the left to the right: galaxies, clusters and AGNs) $b^l_{\rm slope}$ agrees well with the bias calculated by equations (2) and (3) in the large-scale limit, but deviates on small scales. This result confirms that the linear bias gives a good description of the relation between luminous tracers and matter around voids, as long as sufficiently large voids are under study. Hence, computing the slope in equation (12) with a simple linear fit, as described in Section 4.1, provides another technique to estimate the linear bias in simulations, if sufficiently large voids are analysed. Such a technique, in principle, allows us to extend the measurement of linear bias to smaller scales inside voids. A caveat is the large uncertainty: close to void centres Poisson noise increases and we should carefully consider how to further test this extension.

To additionally examine the consistency of our procedure to calculate the bias, we verify how $b_{\rm slope}$ changes after imposing various mass cuts on the cluster sample. Namely, we demand the cluster mass to be $M_{500c} \geq 5 \times 10^{13}$ M$_\odot$ h$^{-1}$ and $M_{500c} \geq 10^{14}$ M$_\odot$ h$^{-1}$. To be conservative, we rerun the void-finding algorithm after applying each selection cut on top of the cluster sample and we repeat the stacking procedure. By imposing these cuts, we include a smaller number of clusters in the analysis (see Table 1), which implies that we are not able to resolve the smallest voids due to the sparsity of the tracers (see e.g. Sutter et al. 2014b). In order to include a sufficient number of voids, we need to modify the binning employed in the stacking procedure. In fact, since we are not able to resolve the smallest voids, it is necessary to remove, shift or enlarge some of the bins. Being able to resolve only very large voids in the sample of clusters with $M_{500c} \geq 10^{14}$ M$_\odot$ $h^{-1}$, we do not expect to find a high accuracy result; however, we aim to find at least a qualitative indication that the bias that we measure using $b^l_{\rm slope}$ increases as expected in this case.

In Fig. 6, we show the distribution of clusters around cluster-void centres as a function of their matter distribution (in analogy to Fig. 3); we are displaying the relation for the largest voids in each sample, i.e. for voids with an $R_{\rm eff}$ in the bin-size range (from the left to the right) of 130–140 , 170–200 and 220–290 Mpc h$^{-1}$. After applying the mass cuts, we are still able to fit the matter–tracer relation with a simple linear dependency (i.e. using equation 12) where the offset value is consistent with zero. The exclusion of low-mass clusters from our main samples increases the noise on our measurement, which is now not as well determined as in Fig. 3: the error bars are larger than in the full cluster-sample case and the simulation points are sometime further away from the fit (dotted line). However, we can clearly see that $b_{\rm slope}$ increases from the left- to the right-hand panels of Fig. 6, following an expected trend,

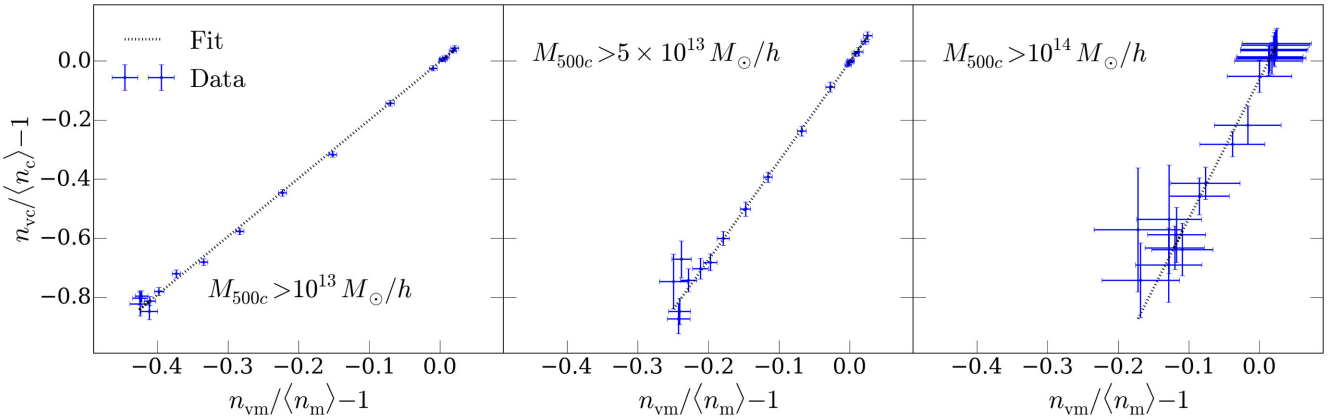


**Figure 6.** Distribution of clusters around cluster-void centres as a function of the matter distribution around cluster voids measured after applying various mass cuts: from the left to the right $M_{500c} > 10^{13}\,M_\odot\,h^{-1}$ (full sample), $M_{500c} > 5\times10^{13}\,M_\odot\,h^{-1}$ and $M_{500c} > 10^{14}\,M_\odot\,h^{-1}$. The measured points (blue) are fitted with a linear function (dotted line) presented in equation (12). The slope increases from the left- to the right-hand panels as expected due to the increasing mass of the objects included in the analysis. We are showing the plot for the largest voids included in each sample, i.e. from left to right for voids with size 130–140, 170–200 and 220–290 Mpc $h^{-1}$.

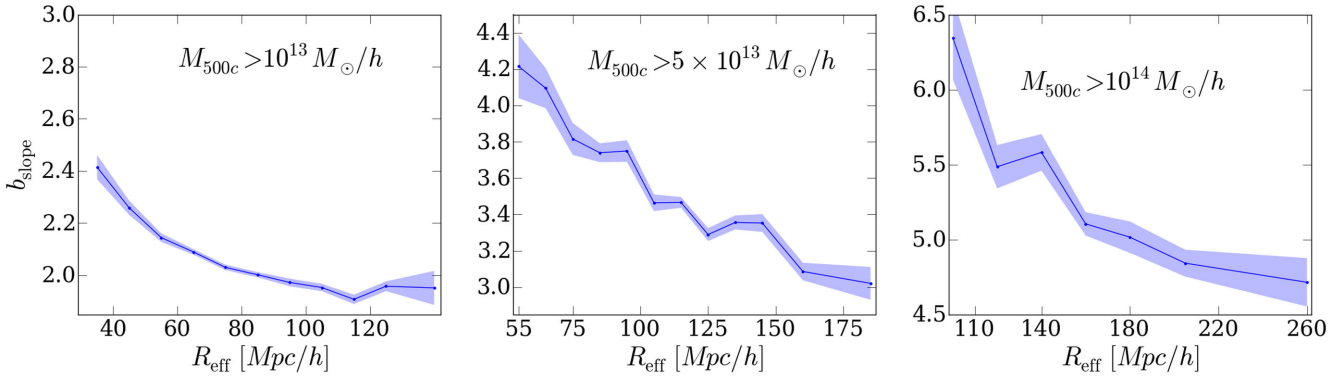


**Figure 7.** Values of $b_{slope}$ after applying different mass cuts on the cluster sample as a function of void size. The shaded area represents the uncertainty, obtained from the error on the fit. In agreement with previous findings we see an impact of void size on the measurement of $b_{slope}$, which becomes largest for small voids. In the cases in which a mass cut is applied (central and right-hand panels, $M_{500c} \geq 5\times10^{13}\,M_\odot\,h^{-1}$ and $M_{500c} \geq 10^{14}\,M_\odot\,h^{-1}$) we observe that $b_{slope}$ decreases as the void size increases, although in a noisy manner. It is also not clear whether the convergence to the value of the linear bias is reached as in the full cluster sample (left-hand panel).

since we are imposing a larger and larger threshold on the mass cut (therefore including only objects with higher and higher bias).

As previously done with the other tracers under study, we performed our analysis on voids of various size. We show how the value of $b_{slope}$ changes as a function of void size in Fig. 7: going from the left to the right, we display the curve for clusters with $M_{500c} \geq 10^{13}\,M_\odot\,h^{-1}$ (same as Fig. 5, central panel, reported here for comparison), $M_{500c} \geq 5\times10^{13}\,M_\odot\,h^{-1}$ and $M_{500c} \geq 10^{14}\,M_\odot\,h^{-1}$. For what concerns the cases in which a mass cut is applied (central and right-hand panels) we see, in agreement with our previous findings, that small voids yield a higher value of $b_{slope}$, although the trend is not as clearly saturating as in the full cluster sample (left-hand panel). For the samples in which clusters have a mass $M_{500c} \geq 5\times10^{13}\,M_\odot\,h^{-1}$ and $M_{500c} \geq 10^{14}\,M_\odot\,h^{-1}$ we were also expecting an increasing critical void size at which $b_{slope}$ converges to a constant value, due both to the inclusion of highly biased tracers and to their increased sparsity. However, in this case $b_{slope}$ does not converge to a constant value. It is therefore not clear whether we resolve voids large enough to reach the convergence value in the central and right-hand panels.

We can now compare $b^l_{slope}$ with the bias calculated using equations (2) and (3). Since we are only considering clusters, we can now include theory predictions to our plot, using the Mo & White formula (equation 4) and its extension by Tinker (equation 6). To estimate the mean value of $b_{MW}$ and $b_{Tinker}$, we use as weight the theoretical mass function calculated with Press & Schechter (1974) and Tinker et al. (2010), respectively.

In Fig. 8, we plot the values of linear bias calculated with all of these methods. Namely:

(i) $b^l_{slope}$ (solid line, the shaded area represents the error on the mean value of $b_{slope}$ for voids of various sizes);
(ii) $b$ from equation (2) (dash–dotted line);
(iii) $b_{MW}$ from equation (4) (long dashed line);
(iv) $b_{Tinker}$ from equation (6) (dashed line).

For the most numerous cluster sample under study ($M_{500c} \geq 10^{13}M_\odot\,h^{-1}$, left-hand panel), we are showing the same plot as Fig. 5 (central panel) for the comparison. In this case and for $M_{500c} \geq 5\times10^{13}\,M_\odot\,h^{-1}$ (central panel), we find a good agreement of $b^l_{slope}$, both with theory and with theoretical bias computed with

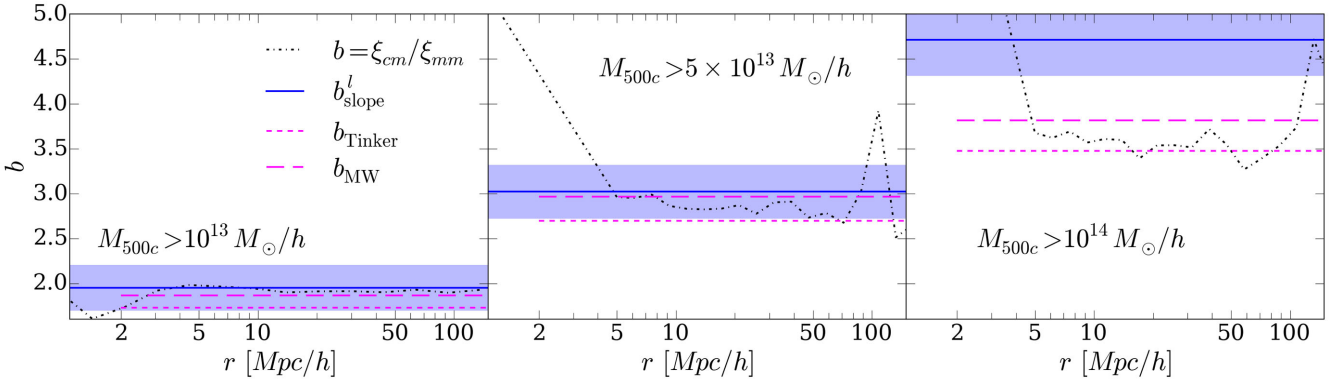


**Figure 8.** Comparison between different bias estimators and theory after applying various mass cuts: we plot the bias of clusters calculated as $b^l_{\rm slope}$ (solid line), and the classical bias estimator (equation (2), dash–dotted line). The value predicted by equations (6) and (4) is shown by the dashed line and the long dashed line, respectively. The shaded areas represent the standard deviation from the mean values of $b_{\rm slope}$.

equations (2) and (3). Values predicted by other bias estimators are within the uncertainty. As we commented before, the agreement is remarkable on large scales while on small scales the traditional bias estimators deviate from $b^l_{\rm slope}$. For what concerns the analysis in the sample which includes only clusters with $M_{500c} > 10^{14} {\rm M}_\odot\, h^{-1}$ (right-hand panel), we see a significant deviation of $b^l_{\rm slope}$ from other bias predictions. We expected the latter case to be the most problematic, given the large noise due to the extreme mass cut applied (see Table 1). Besides this, there is a practical motivation for such a discrepancy: as we suspected, we did not resolve enough large voids to determine the convergence of $b_{\rm slope}$. We are, in fact, forced to include voids of a wide range of sizes in the bin that contains the largest voids in this sample (220–290 Mpc h$^{-1}$) in order to obtain sufficiently smooth profiles and reach the convergence in the linear fit between matter-void profile and cluster-void density profile. This is absolutely necessary: if we would include only voids with sizes between, e.g. 225 and 290 Mpc h$^{-1}$, the linear fit would not converge. Apparently, for this particular case, voids with $R_{\rm eff} \approx 220$ Mpc h$^{-1}$ are too small to attain the convergence of $b_{\rm slope}$ to the value of the linear bias. Ideally, if we had resolved a sufficient number of very large voids ($R_{\rm eff} > 250$ Mpc h$^{-1}$), we would recover the value of the linear bias also in this case, but the simulation box is too small to get a sufficiently large number of voids of that size. This is indeed a critical point as, the only way to tell if $b_{\rm slope}$ converged to a saturated value is by looking at Figs 4 and 7. Moreover, for practical purposes we can use the relative bias between different tracers for that matter, which is accessible in observations.

As we commented before, it is not clear by Fig. 7 whether $b_{\rm slope}$ converges to a constant value for the cluster samples with $M_{500c} \geq 5 \times 10^{13}$ M$_\odot$ h$^{-1}$ and $M_{500c} \geq 10^{14}$ M$_\odot$ h$^{-1}$: looking at Fig. 8, we can conclude that the convergence is reached for $M_{500c} \geq 5 \times 10^{13}$ M$_\odot$ h$^{-1}$ but not for the most extreme mass cut. It is remarkable that, in the latter case, we understand why the convergence of $b^l_{\rm slope}$ cannot occur. However, we have demonstrated that our method of calculating the bias with $b^l_{\rm slope}$ is quite consistent when applied on samples with various masses, which was the aim of this test.

To summarize this section, we have shown that the relation between matter and matter–tracers in voids is always linear and determined by a single number $b_{\rm slope}$. This result was established by directly measuring the distribution of matter and tracers around voids and incidentally validates recent work that simply assumed the bias of tracers to be linear in the vicinity of voids. Furthermore, we showed that, by measuring the matter profile and the matter–tracer profiles around large voids in simulations, we can estimate the value of the linear bias via the slope of a simple linear fit between the two distributions, if sufficiently large voids are considered.

## 5 DISCUSSION AND CONCLUSIONS

With the help of a suite of state-of-the-art hydro-simulations, we have investigated the stacked tracer-density profile of cosmic voids and linked it to their underlying matter-density profile. Before discussing the implications of our findings, we recap all major results of this work:

(i) *The underlying matter-density profile of tracer-voids is well described by the fitting formula presented in Hamaus et al. (2014c).* Such a formula was known to describe the profile of tracer-voids and matter-voids separately, but in this work we have successfully tested it on depressions of the matter-density field around tracer-voids, i.e. without running the void finder on dark matter particles. This result points out once again the degree of self-similarity of underdense regions in our Universe, as they can always be described by the same fitting function.

(ii) *The relation between the density of tracers and matter around voids is always linear and determined by a multiplicative constant* ($b_{\rm slope}$). This remarkably simple relation was tested using galaxy, cluster and AGN samples extracted from *Magneticum Pathfinder*, including voids of various sizes and applying different mass cuts on top of the cluster sample. The linear relation between matter and tracers always stands, regardless of tracer type and host-halo mass range.

(iii) *The value of the multiplicative constant decreases with the increase of the size of voids and asymptotes to the linear bias.* For sufficiently large voids, $b_{\rm slope}$ is shown to match the linear bias extracted from the usual tracer auto-correlation, the tracer cross-correlation with dark matter, and the expectations from theory, such as the bias functions proposed by Mo&White and Tinker. The critical void size at which $b_{\rm slope}$ converges to the linear bias is dependent on the clustering properties of the tracers under study (and on their sparsity). In fact, we find that for the full cluster sample the critical void size is around 80 Mpc h$^{-1}$ while for AGNs it is around 60 Mpc h$^{-1}$ and for galaxies about 50 Mpc h$^{-1}$. In order to eliminate the effect of sparsity, we sub-sampled all tracers to the density of our full cluster sample. This test reveals that the critical void

size at which $b_{\rm slope}$ reaches a saturated value also depends on tracer properties other than density, such as their bias. If a highly biased and very sparse population is used as tracer of the density field, it can be possible that not enough large voids are available and hence we cannot establish the constant value to which $b_{\rm slope}$ converges. The large values of $b_{\rm slope}$ obtained by small voids show that they yield a biased result. We leave further investigations on the origin of this effect to future studies.

The correspondence between $b_{\rm slope}$ and linear bias is expected at linear order in the density fluctuations, because we can consider the stacked tracer-density profile of voids as a void–tracer cross-correlation function $\xi_{\rm vt}(r)$ (see equation 11), and express it in terms of the void-matter cross-correlation function,

$$\xi_{\rm vt}(r) = b\xi_{\rm vm}(r), \tag{13}$$

via the linear tracer bias $b$. We find that equation (13) is in principle valid for arbitrarily small values of $r$, as long as large enough voids are considered, in stark contrast to the common two-point statistics of tracers appearing in equations (2) and (3). For the latter, the linear bias model can break down below scales of the order of $\sim$50 Mpc h$^{-1}$ at low redshift and is therefore not applicable for a dominant fraction of available Fourier modes of the density field.

Furthermore, this technique can yield important advantages for the analysis of survey data. In order to maximize the amount of cosmological information contained within the common two-point statistics of large-scale structure, one has to make use of sophisticated perturbation theory frameworks to consistently include all higher-order bias parameters (e.g. Fry & Gaztanaga 1993; McDonald & Roy 2009; Beutler et al. 2017; Sánchez et al. 2017b). Alternatively, one can marginalize over the unknown free parameters of an empirical function that models non-linear bias in a phenomenological way. However, both approaches are very limited; they quickly break down towards smaller scales and the total information gain does not scale with the additional number of modes included.

As long as tracer bias remains scale-independent, as shown to be the case in void–tracer cross-correlations, these limitations do not apply. An example for such a cosmological analysis is the study of redshift-space distortions around voids (Hamaus et al. 2015, 2016; Cai et al. 2016; Chuang et al. 2016; Hawken et al. 2016; Achitouv et al. 2017), but the interpretation of many other observables, such as void abundance, void lensing, void clustering and the void ISW effect, may benefit from a linear bias treatment as well. An exciting perspective is to look out for additional physical effects that induce a non-linear scale-dependent tracer bias around voids, and are typically neglected in standard ΛCDM. One such example is the effect of massive neutrinos (LoVerde 2014; Castorina et al. 2015; Banerjee & Dalal 2017; Carbone, Petkova & Dolag 2016). Similar signatures can be expected in scenarios of modified gravity (Cai et al. 2015; Achitouv et al. 2016) or coupled DE (Pollina et al. 2016). We leave further research along these lines for future work.

## ACKNOWLEDGEMENTS

We are thankful to Paul Sutter, Guilhem Lavaux and Steffen Hagstotz for useful discussions. KD and JW acknowledge the support of the DFG Cluster of Excellence 'Origin and Structure of the Universe' and the Transregio programme TR33 'The Dark Universe'. MB acknowledges support from the Italian Ministry for Education, University and Research (MIUR) through the SIR individual grant SIMCODE, project number RBSI14P4IH. LM acknowledges financial contribution from the agreement ASI n.I/023/12/0 'Attivitá relative alla fase B2/C per la missione Euclid'. The calculations have partially been carried out on the computing facilities of the Computational Center for Particle and Astrophysics (C2PAP) and of the Leibniz Supercomputer Center (LRZ) under the project IDs pr58we, pr83li and pr86re. Special thanks go to LRZ for the opportunity to run the Box0 simulation within the Extreme Scale-Out Phase on the new SuperMUC Haswell extension system. We appreciate the support from the LRZ team, especially N. Hammer, when carrying out the Box0 simulation.

## REFERENCES

Achitouv I., Baldi M., Puchwein E., Weller J., 2016, Phys. Rev. D, 93, 10
Achitouv I., Neyrinck M., Paranjape A., 2015, MNRAS, 451, 3964
Achitouv I., Blake C., Carter P., Koda J., Beutler F., 2017, Phys. Rev. D, 92, 8
Alcock C., Paczynski B., 1979, Nature, 281, 358
Amendola L. et al., 2013, Living Rev. Relativ., 16, 6
Baldi M., Villaescusa-Navarro F., 2016, MNRAS, preprint (arXiv:1608.08057)
Banerjee A., Dalal N., 2016, JCAP, preprint (arXiv:1606.06167)
Barreira A., Cautun M., Li B., Baugh C. M., Pascoli S., 2015, J. Cosmol. Astropart. Phys., 8, 28
Beutler F. et al., 2017, MNRAS, 466, 2242
Blumenthal G. R., da Costa L. N., Goldwirth D. S., Lecar M., Piran T., 1992, ApJ, 388, 234
Bocquet S., Saro A., Dolag K., Mohr J. J., 2016, MNRAS, 456, 2361
Bond J. R., Cole S., Efstathiou G., Kaiser N., 1991, ApJ, 379, 440
Bond J. R., Kofman L., Pogosyan D., 1996, Nature, 380, 603
Bos E. G. P., van de Weygaert R., Dolag K., Pettorino V., 2012, MNRAS, 426, 440
Cai Y.-C., Padilla N., Li B., 2015, MNRAS, 451, 1036
Cai Y.-C., Taylor A., Peacock J. A., Padilla N., 2016, MNRAS, 462, 2465
Carbone C., Petkova M., Dolag K., 2016, J. Cosmol. Astropart. Phys., 7, 034
Castorina E., Carbone C., Bel J., Sefusatti E., Dolag K., 2015, J. Cosmol. Astropart. Phys., 7, 043
Cautun M., van de Weygaert R., Jones B. J. T., Frenk C. S., 2014, MNRAS, 441, 2923
Ceccarelli L., Paz D., Lares M., Padilla N., Lambas D. G., 2013, MNRAS, 434, 1435
Chabrier G., 2003, PASP, 115, 763
Chan K. C., Hamaus N., Desjacques V., 2014, Phys. Rev. D, 90, 103521
Chuang C.-H., Kitaura F.-S., Liang Y., Font-Ribera A., Zhao C., McDonald P., Tao C., 2016, preprint (arXiv:1605.05352)
Clampitt J., Jain B., 2015, MNRAS, 454, 3357
Clampitt J., Cai Y.-C., Li B., 2013, MNRAS, 431, 749
Clampitt J., Jain B., Sánchez C., 2016, MNRAS, 456, 4425
Colberg J. M., Sheth R. K., Diaferio A., Gao L., Yoshida N., 2005, MNRAS, 360, 216
Colberg J. M. et al., 2008, MNRAS, 387, 933
D'Amico G., Musso M., Noreña J., Paranjape A., 2011, Phys. Rev. D, 83, 023521
Demchenko V., Cai Y.-C., Heymans C., Peacock J. A., 2016, MNRAS, 463, 512
Di Matteo T., Springel V., Hernquist L., 2005, Nature, 433, 604
Dolag K., Jubelgas M., Springel V., Borgani S., Rasia E., 2004, ApJ, 606, L97
Dolag K., Vazza F., Brunetti G., Tormen G., 2005, MNRAS, 364, 753
Dolag K., Borgani S., Murante G., Springel V., 2009, MNRAS, 399, 497
Dolag K., Gaensler B. M., Beck A. M., Beck M. C., 2015, MNRAS, 451, 4277
Dolag K., Komatsu E., Sunyaev R., 2016, MNRAS, 463, 1797

Eke V. R., Cole S., Frenk C. S., 1996, MNRAS, 282, 263
Elyiv A., Marulli F., Pollina G., Baldi M., Branchini E., Cimatti A., Moscardini L., 2015, MNRAS, 448, 642
Fabjan D., Borgani S., Tornatore L., Saro A., Murante G., Dolag K., 2010, MNRAS, 401, 1670
Falck B., Neyrinck M. C., 2015, MNRAS, 450, 3239
Finelli F., García-Bellido J., Kovács A., Paci F., Szapudi I., 2014, Proc. IAU Symp. 306, Statistical Challenges in 21st Century Cosmology. Cambridge Univ. Press, Cambridge, p. 163
Fry J. N., Gaztanaga E., 1993, ApJ, 413, 447
Gibbons G. W., Werner M. C., Yoshida N., Chon S., 2014, MNRAS, 438, 1603
Gregory S. A., Thompson L. A., Tifft W. G., 1978, BAAS, 10, 622
Gruen D. et al., 2016, MNRAS, 455, 3367
Hamaus N., Sutter P. M., Lavaux G., Wandelt B. D., 2014a, J. Cosmol. Astropart. Phys., 12, 013
Hamaus N., Wandelt B. D., Sutter P. M., Lavaux G., Warren M. S., 2014b, Phys. Rev. Lett., 112, 041304
Hamaus N., Sutter P. M., Wandelt B. D., 2014c, Phys. Rev. Lett., 112, 251302
Hamaus N., Sutter P. M., Lavaux G., Wandelt B. D., 2015, J. Cosmol. Astropart. Phys., 11, 036
Hamaus N., Pisani A., Sutter P. M., Lavaux G., Escoffier S., Wandelt B. D., Weller J., 2016, Phys. Rev. Lett., 117, 091302
Hausman M. A., Olson D. W., Roth B. D., 1983, ApJ, 270, 351
Hawken A. J. et al., 2016, Proc. IAU Symp. 308, The Zeldovich Universe: Genesis and Growth of the Cosmic Web. Cambridge Univ. Press, Cambridge, p. 571
Hirschmann M., Dolag K., Saro A., Bachmann L., Borgani S., Burkert A., 2014, MNRAS, 442, 2304
Izumi K., Hagiwara C., Nakajima K., Kitamura T., Asada H., 2013, Phys. Rev. D, 88, 024049
Jennings E., Li Y., Hu W., 2013, MNRAS, 434, 2167
Kaiser N., 1984, ApJ, 284, L9
Kirshner R. P., Oemler Jr. A., Schechter P. L., Shectman S. A., 1981, ApJ, 248, L57
Kitaura F.-S. et al., 2016, Phys. Rev. Lett., 116, 171301
Komatsu E. et al., 2011, ApJS, 192, 18
Kovács A., García-Bellido J., 2016, MNRAS, 462, 1882
Kovács A., Granett B. R., 2015, MNRAS, 452, 1295
Kovač K. et al., 2014, MNRAS, 438, 717
Krause E., Chang T.-C., Doré O., Umetsu K., 2013, ApJ, 762, L20
Laureijs R. et al., 2011, preprint (arXiv:1110.3193)
Lavaux G., Wandelt B. D., 2010, MNRAS, 403, 1392
Lavaux G., Wandelt B. D., 2012, in American Astronomical Society Meeting Abstracts 219. p. 336.02
Li B., 2011, MNRAS, 411, 2615
Liang Y., Zhao C., Chuang C.-H., Kitaura F.-S., Tao C., 2016, MNRAS, 459, 4020
LoVerde M., 2014, Phys. Rev. D, 90, 083530
Mao Q. et al., 2017, ApJ, 835, 161
McDonald P., Roy A., 2009, J. Cosmol. Astropart. Phys., 8, 020
McDonald M. et al., 2014, ApJ, 794, 67
Massara E., Villaescusa-Navarro F., Viel M., Sutter P. M., 2015, J. Cosmol. Astropart. Phys., 11, 018
Melchior P., Sutter P. M., Sheldon E. S., Krause E., Wandelt B. D., 2014, MNRAS, 440, 2922
Mo H. J., White S. D. M., 1996, MNRAS, 282, 347
Nadathur S., 2016, MNRAS, 461, 358
Nadathur S., Hotchkiss S., 2015a, MNRAS, 454, 889
Nadathur S., Hotchkiss S., 2015b, MNRAS, 454, 2228
Nadathur S., Lavinto M., Hotchkiss S., Räsänen S., 2014, Phys. Rev. D, 90, 103510
Naidoo K., Benoit-Lévy A., Lahav O., 2016, MNRAS, 459, L71
Neyrinck M. C., 2008, MNRAS, 386, 2101
Odrzywołek A., 2009, Phys. Rev. D, 80, 103515
Padilla N. D., Ceccarelli L., Lambas D. G., 2005, MNRAS, 363, 977
Pan D. C., Vogeley M. S., Hoyle F., Choi Y.-Y., Park C., 2012, MNRAS, 421, 926
Peebles P. J. E., 1980, The Large-scale Structure of the Universe. Princeton Univ. Press, Princeton, NJ
Pisani A., Sutter P. M., Hamaus N., Alizadeh E., Biswas R., Wandelt B. D., Hirata C. M., 2015, Phys. Rev. D, 92, 083531
Planck Collaboration V et al., 2013, A&A, 550, A131
Platen E., van de Weygaert R., Jones B. J. T., 2007, MNRAS, 380, 551
Pogosyan D., Bond J. R., Kofman L., Wadsley J., 1998, in Colombi S., Mellier Y., Raban B., eds, Wide Field Surveys in Cosmology. Editions Frontieres, Paris, p. 61
Pollina G., Baldi M., Marulli F., Moscardini L., 2016, MNRAS, 455, 3075
Press W. H., Schechter P., 1974, ApJ, 187, 425
Pycke J.-R., Russell E., 2016, ApJ, 821, 110
Rees M. J., Sciama D. W., Stobbs S. H., 1968, Astrophys. Lett., 2, 243
Remus R.-S., Burkert A., Dolag K., Johansson P. H., Naab T., Oser L., Thomas J., 2013, ApJ, 766, 71
Remus R.-S., Burkert A., Dolag K., 2017, Proc. IAU Symp. 321, Formation and Evolution of Galaxy Outskirts. Cambridge Univ. Press, Cambridge, p. 84
Ricciardelli E., Quilis V., Planelles S., 2013, MNRAS, 434, 1192
Ricciardelli E., Quilis V., Varela J., 2014, MNRAS, 440, 601
Sánchez C. et al., 2017a, MNRAS, 465, 746
Sánchez A. G. et al., 2017b, MNRAS, 464, 1640
Saro A. et al., 2014, MNRAS, 440, 2610
Seljak U., Warren M. S., 2004, MNRAS, 355, 129
Sheth R. K., Tormen G., 1999, MNRAS, 308, 119
Sheth R. K., Tormen G., 2002, MNRAS, 329, 61
Sheth R. K., van de Weygaert R., 2004, MNRAS, 350, 517
Sheth R. K., Mo H. J., Tormen G., 2001, MNRAS, 323, 1
Spitzer L., 1962, Physics of Fully Ionized Gases
Springel V., 2005, MNRAS, 364, 1105
Springel V., Hernquist L., 2002, MNRAS, 333, 649
Springel V., Hernquist L., 2003, MNRAS, 339, 289
Springel V., White S. D. M., Tormen G., Kauffmann G., 2001, MNRAS, 328, 726
Springel V., Di Matteo T., Hernquist L., 2005, MNRAS, 361, 776
Steinborn L. K., Dolag K., Hirschmann M., Prieto M. A., Remus R.-S., 2015, MNRAS, 448, 1504
Steinborn L. K., Dolag K., Comerford J. M., Hirschmann M., Remus R.-S., Teklu A. F., 2016, MNRAS, 458, 1013
Sutter P. M., Lavaux G., Wandelt B. D., Weinberg D. H., 2012a, ApJ, 761, 44
Sutter P. M., Lavaux G., Wandelt B. D., Weinberg D. H., 2012b, ApJ, 761, 187
Sutter P. M., Lavaux G., Wandelt B. D., Weinberg D. H., Warren M. S., 2014a, MNRAS, 438, 3177
Sutter P. M., Lavaux G., Hamaus N., Wandelt B. D., Weinberg D. H., Warren M. S., 2014b, MNRAS, 442, 462
Sutter P. M., Pisani A., Wandelt B. D., Weinberg D. H., 2014c, MNRAS, 443, 2983
Sutter P. M. et al., 2015, Astron. Comput., 9, 1
Teklu A. F., Remus R.-S., Dolag K., Beck A. M., Burkert A., Schmidt A. S., Schulze F., Steinborn L. K., 2015, ApJ, 812, 29
Tinker J. L., Robertson B. E., Kravtsov A. V., Klypin A., Warren M. S., Yepes G., Gottlöber S., 2010, ApJ, 724, 878
Tornatore L., Borgani S., Dolag K., Matteucci F., 2007, MNRAS, 382, 1050
Wiersma R. P. C., Schaye J., Smith B. D., 2009, MNRAS, 393, 99
Wojtak R., Powell D., Abel T., 2016, MNRAS, 458, 4431
Zentner A. R., 2007, Int. J. Modern Phys. D, 16, 763
Zivick P., Sutter P. M., Wandelt B. D., Li B., Lam T. Y., 2015, MNRAS, 451, 4215

This paper has been typeset from a TEX/LATEX file prepared by the author.